Biointerphases
A Journal of Biomaterials and Biological Interfaces

Composition controls soft hydrogel surface layer dimensions and contact mechanics F

Cite as: Biointerphases **17**, 061002 (2022); https://doi.org/10.1116/6.0002047
Submitted: 29 June 2022 • Accepted: 23 September 2022 • Published Online: 07 November 2022

Christopher L. Johnson and Alison C. Dunn

COLLECTIONS

Paper published as part of the special topic on Special Topic Collection: Polymeric Biointerfaces A Collection in celebration of Nicholas D. Spencers career

F This paper was selected as Featured

Biointerphases
A Journal of Biomaterials and Biological Interfaces

ARTICLE

avs.scitation.org/journal/bip

Composition controls soft hydrogel surface layer dimensions and contact mechanics

Cite as: Biointer*phases* **17**, 061002 (2022); doi: 10.1116/6.0002047
Submitted: 29 June 2022 · Accepted: 23 September 2022 ·
Published Online: 7 November 2022

View Online Export Citation CrossMark

Christopher L. Johnson and Alison C. Dunn[a)]

AFFILIATIONS

Department of Mechanical Science and Engineering, University of Illinois at Urbana-Champaign, Urbana, Illinois 61801

Note: This paper is part of the Biointerphases Special Topic Collection on Polymeric Biointerfaces A collection in celebration of Nicholas D. Spencers career.

[a)] **Author to whom correspondence should be addressed:** acd@illinois.edu

ABSTRACT

Hydrogels are soft hydrated polymer networks that are widely used in research and industry due to their favorable properties and similarity to biological tissues. However, it has long been difficult to create a hydrogel emulating the heterogeneous structure of special tissues, such as cartilage. One potential avenue to develop a structural variation in a hydrogel is the "mold effect," which has only recently been discovered to be caused by absorbed oxygen within the mold surface interfering with the polymerization. This induces a dilute gradient-density surface layer with altered properties. However, the precise structure of the gradient-surface layer and its contact response have not yet been characterized. Such knowledge would prove useful for designs of composite hydrogels with altered surface characteristics. To fully characterize the hydrogel gradient-surface layer, we created five hydrogel compositions of varying monomer and cross-linker content to encompass variations in the layer. Then, we used particle exclusion microscopy during indentation and creep experiments to probe the contact response of the gradient layer of each composition. These experiments showed that the dilute structure of the gradient layer follows evolving contact behavior allowing poroelastic squeeze-out at miniscule pressures. Stiffer compositions had thinner gradient layers. This knowledge can potentially be used to create hydrogels with a stiff load-bearing bulk with altered surface characteristics tailored for specific tribological applications.

I. INTRODUCTION

Hydrogels are a special case of polymer gels where the pores of the gel are occupied by water molecules. This is made possible due to the affinity of the polymer backbone to hydrogen bond with water, causing the network to trap a comparatively large amount of water compared to its own weight.[1] One of the most commonly used hydrogels is the polyacrylamide (pAam) chemically cross-linked hydrogel system, which, at an equilibrium state, can be comprised of up to 95% water by mass.[2] Due to their biocompatibility and lubricity, hydrogels are one of the best materials for directly interfacing with or replacing tissues within the human body.[3–6] Additionally, their biphasic composition resembles that of many biological tissues, such as cartilage. Because of this, hydrogels are frequently researched and used in biomedical applications, such as scaffolding for tissue growth, and liners of medical devices.[7,8] Many of these applications involve dynamic interfaces: for example, hydrogels have been heavily studied and used as low-friction contact lenses that interface directly with the eye.[9–15] There has also been a significant body of work surrounding the use of a hydrogel system as artificial cartilage.[16–23] However, cartilage is a complex heterogeneous material that has proven difficult to emulate with synthetic formulations. Cartilage exhibits a distinct compositelike heterogeneous structure that allows it to out-perform most hydrogels in lubricity and strength.[6,23–25] Cartilage, and any surrogate, must be able to support impact and sustained loads of the weight of a human, while also maintaining sufficient lubrication between sliding joints without experiencing significant wear. This has been the largest issue for hydrogels as cartilage replacement thus far—no hydrogel formulation has been able to achieve the delicate balance of high stiffness and wear resistance while maintaining high lubricity. There have been a number of novel attempts to address this open challenge, including interpenetrating networks for improved bulk moduli,[23,26–28] compositing with secondary elements,[29,30] or deposition of a less-dense structure atop a bulk.[31]

However, these approaches introduce numerous complexities to hydrogel manufacturing and synthesis without fully solving the heterogeneous structure issue.

One unexplored yet simple method to alter the mechanical and tribological properties of a hydrogel is the "mold effect," where the material of the mold alters the polymer structure of the hydrogel. The first mention of the potential effect of the mold material on the resulting mechanical or tribological behavior of a hydrogel was brought up by Kii and Gong in 2001, who believed it to be due to the hydrophobicity of the mold surface.[32,33] However, it was not until recently that the mold effect of chemically cross-linked hydrogels was actively investigated. Meier *et al.* showed that the choice of the mold material impacts the stiffness of the first few micrometers of the hydrogel, with certain mold materials, particularly polymers, producing weaker force responses per indentation depth.[34] Characterization of these hydrogels using neutron reflectometry and infrared spectroscopy revealed that the choice of the mold material does influence the degree of cross-linking of the gel closest to the mold surface to create a "brushy" surface layer on the order of 10–20 μm thick.[35] Very recent work by Simič found that the mold effect is due to the available oxygen at the surface during polymerization, with latent oxygen within polymer materials inducing the dilute soft surface layer.[36] All of these observations support the notion that the surface structure is highly dependent on the choice of the mold material. However, we aim to systematically describe the quantitative relationship between bulk composition and the structure of the resulting surface layer, which is more readily controlled than the oxygen environment at the mold surfaces.

We hypothesize that the oxidation polymerization and simultaneous cross-linking occurring at the boundary of the hydrogel prepolymer and the mold surface create a structurally gradient surface. We specifically propose that the structure is defined by the kinetics of this reaction as it occurs with the available monomer and cross-linker concentrations in the solution. By performing studies focused on the effect of the gradient layer and variations in its thickness with respect to prepolymer composition, we can determine practical controls for the gradient-surface layer with respect to these compositional levers. This knowledge can then be utilized to easily generate heterogeneous hydrogel structures mimicking complex tissues. In this present work, we conducted a thorough contact mechanics characterization of pAam hydrogels possessing a significant less-dense gradient layer imparted by a Polystyrene (PS) mold material (Fig. 1). Five sample compositions are produced changing both the total polymer percent M as well as the monomer-to-cross-linker ratio R to determine the influence of both metrics. Using instrumented tribometry combined with particle exclusion contact area visualization, we found how contact mechanics of the altered surface can be described using a piecewise contact model approach representing the evolving structure of the gradient surface with probe penetration depth. Creep experiments show that all but the most dilute polymer compositions can experience poroelastic relaxation locally within the gradient-surface layer due to the lower degree of cross-linking. Last, we provide an estimate of the thickness of each composition's gradient layer and show that the monomer-to-cross-linker ratio R is more critical in determining the thickness of this layer. These findings provide direct links between the gradient-surface layer and the bulk composition, allowing predictive design of heterogeneous hydrogel structures. This also establishes a framework for future tribological studies focused on the friction and lubrication of gradient-surface layers.

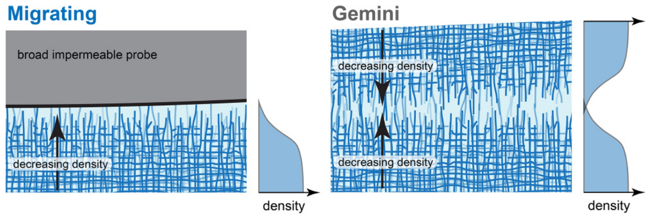

FIG. 1. Illustration of the two contact types used for all experiments in this work: migrating (also known as "soft-substrate") and self-mated contact (referred to as "Gemini" contact). By molding against PS, these hydrogels develop the gradient-density surface layer.

II. MATERIALS AND METHODS

A. Hydrogel preparation

pAam hydrogels were created using stock solutions of an acrylamide (Aam) monomer, a methylenebisacrylamide (BisAam) cross-linker, tetramethylethylenediamine (TEMED), and ammonium persulfate (APS). These solutions were combined to create a prepolymerized solution that was quickly poured into cylindrical polystyrene molds of diameter 35 mm and height 4 mm and then covered with a polystyrene surface in contact with the solution. After allowing the gels to cure in the mold for 45 min, the gels were cut down to a 25 mm diameter and placed in a de-ionized (DI) water bath for three to five days prior to testing.

Previous work on chemically cross-linked hydrogels has found that variations in either the monomer percent or the ratio of monomer to cross-linker have significant effects on the contact and lubrication responses.[37–45] For this reason, we conducted experiments on five different hydrogel compositions in order to perceive the effects of both metrics. These hydrogels were created by altering the amount of the Aam monomer and the BisAam cross-linker stock solution used during the polymerization. The five compositions and their corresponding wt./wt. % of each constituent are shown in Table I. Of these five compositions, three spanned

TABLE I. Polyacrylamide hydrogel compositions listed by number and wt./wt. % of constituents. Compositions 1, 3, and 5 span variations in the monomer-to-cross-linker ratio R, while compositions 2–4 have varying monomer percent M but a fixed ratio R. All compositions used 0.15 wt. %/wt. TEMED and APS.

Comp no.	M/C ratio R	Monomer % M	Cross-linker % C	Water (%)
1	250	7.5	0.03	92.2
2	25	5	0.2	94.5
3	25	7.5	0.3	91.9
4	25	15	0.6	84.1
5	15	7.5	0.5	91.7

variations in the monomer-to-cross-linker ratio, termed R, while keeping a constant monomer percent of $M = 7.5\%$ (compositions 1, 3, and 5). Three compositions also spanned different monomer percents M while retaining a constant monomer-to-cross-linker ratio of $R = 25$ (compositions 2–4). Compositions 1–4 were transparent, while composition 5 was translucent. This translucence, which colored the hydrogel milky-white, did not visibly impact the accuracy of the contact area measurements. However, further decreases to R would prevent measurement of the contact area using microscopy techniques. Compositions 1 and 2 had the greatest degree of swelling, while compositions 3–5 exhibited insignificant swelling. Composition 1 was expected to be primarily viscoelastic based on previous studies.[46]

The indenting probe material consisted of either a 4 mm diameter steel spherical ball bearing or a 4 mm diameter hydrogel hemisphere. The rigid steel bearing was covered with a single coating of a matte black acrylic paint, which eliminated any light reflection that would reduce image quality. Both probe types were attached to 10 mm long threaded aluminum rods. To create hydrogel probes, we poured the prepolymerized solution into a custom-made mold of Delrin and polyolefin plastic parts. After 30 min, the probe was removed from the mold and allowed to equilibrate in DI water for three to five days. The probe size was constrained to a 4 mm diameter based on the size of the hydrogel probe mold. Previous indentation experiments on hydrogels created using the custom polyolefin copolymer mold piece show that it induces a gradient layer with a similar response as molding against polystyrene.[47] This causes the Gemini contact interface to be a "brushy-brushy" interaction between two gradient-layered hydrogels.

B. Experimental setup

All experiments used an experimental setup consisting of a microtribometer mounted atop an inverted confocal fluorescence microscope (see Fig. 2). Two contact types were tested: a rigid spherical probe indenting into a flat hydrogel surface ("soft-substrate" contact) and a hydrogel hemispherical probe indenting into a flat hydrogel slab ("Gemini" contact[48]) (Fig. 1). This setup was identical to the setup used for previous work conducted by the authors.[47] A detailed description of the tribometer specifications is available in the supplementary material.[68]

C. Particle exclusion microscopy

In order to view contact area projections using the microtribometer setup described above, we required a technique that made use of our confocal microscope. Previous contact imaging techniques on hydrogels have attempted confocal stack imaging[49] as well as a 2D contact area projection through particle exclusion microscopy.[50] We employed a method based loosely off the latter technique to measure contact areas throughout this work, which instead used 1 μm microfluorescent particles in solution as the excluded particles. This method was used in previous studies of these graded hydrogels.[47] In brief, the technique uses average representative images as backgrounds that are subtracted to produce a defined contact border (Fig. 3). Further details regarding the technique are discussed in the supplementary material.[68]

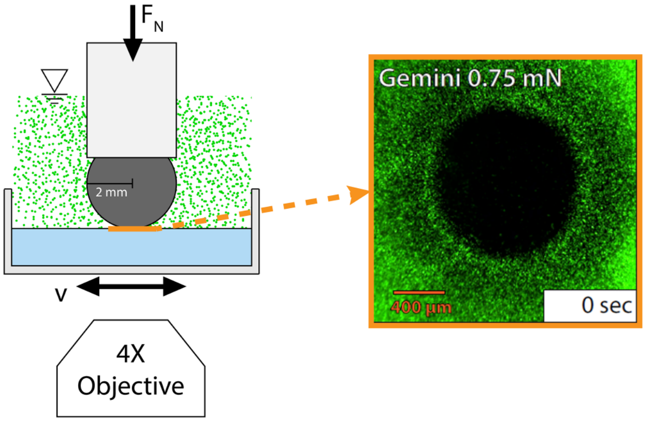

FIG. 2. On the left is shown the particle exclusion setup utilizing a microtribometer mounted atop an inverted confocal microscope. The probe is a 2 mm radius steel ball bearing coated with a matte hydrophobic paint. The water bath consisted of a dilute solution with 1 μm green fluorescent particles. A soft-substrate contact setup is shown—Gemini contact instead uses a hydrogel hemispherical probe. On the right is an example of an image obtained using the particle exclusion technique. The circular region devoid of particles corresponds to the contact area. The experiment was a creep test conducted in a Gemini contact setup with a normal load of 750 μN.

D. Experimental procedure and analysis methods

1. Indentation

Short-duration, displacement-controlled indentation was performed using the tribometer. Indent and pull-off speed was set to 25 μm/s; dwell time was kept to zero. Indentations were performed reaching peak loads of 500, 750, or 1000 μN. Normal force and stage displacement were acquired at a rate of 100 Hz. The force signal error ranged from ± 4 to 18 μN, with the larger error occurring when out of contact. Experiments were performed on areas of the gel at least 4 mm away from each other, with 10 min in between indentations to allow the gel to fully re-equilibrate. Each experiment was repeated three times at different locations on the hydrogel.

Contact area videos were acquired for each indent and then anchored together with the force/displacement data by matching the time of maximum indent depth to the time of maximum contact area. Video snapshots were extracted at 0.3–0.5 s intervals and analyzed for the contact area. The time of first contact in each video was marked for each experiment. Nominal contact pressures were calculated as $P = F_N/A$ using the tribometer-obtained normal force F_N at the time corresponding to the particular contact area A.

Indentation analysis typically involves curve-fitting of a contact model to determine both the reduced modulus and the initial point of contact. For example, in the Hertzian contact model [Eq. (1)], the force response F is dependent on the probe geometry R and the reduced modulus E^* [Eq. (2)] as well as the probe depth at first contact d_o, which are solved for simultaneously. However, traditional indentation analysis techniques pose a challenge when

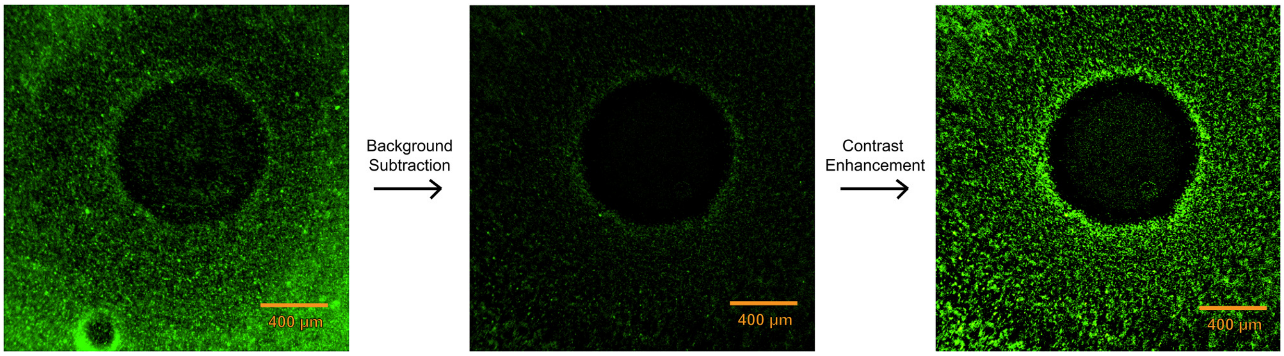

FIG. 3. (left) Example of a raw frame from a creep experiment. (center) The same frame after subtracting a representative background from image stack averaging. (right) Image after contrast enhancement in order to improve the contact boundary.

initial contact does not provoke a strong force response. In very dilute or graded materials, the point of first contact is confounded by a weak force magnitude and poor fitting to established contact models; this has been demonstrated in the previous hydrogel work by the authors.[47] Because both aspects apply to hydrogels with gradient-surface layers, we instead analyzed indentation experiment data using a force-derivative method developed by Garcia *et al.*[51] Using this analysis method, the force-depth power relationship of the raw data is emphasized, particularly for low contact penetration. This allows more accurate fitting of portions of the data to a given contact model, such as Hertzian or Winkler contact. Once the appropriate contact model is determined, a reduced modulus can be calculated independent of the depth of first contact. The portion-based fitting of each indentation can be easily verified against analytic models in a log-log plot of the force derivative versus force (Fig. 4). A deeper explanation of the Garcia analysis method and its application to our data is described in the supplementary material,[68]

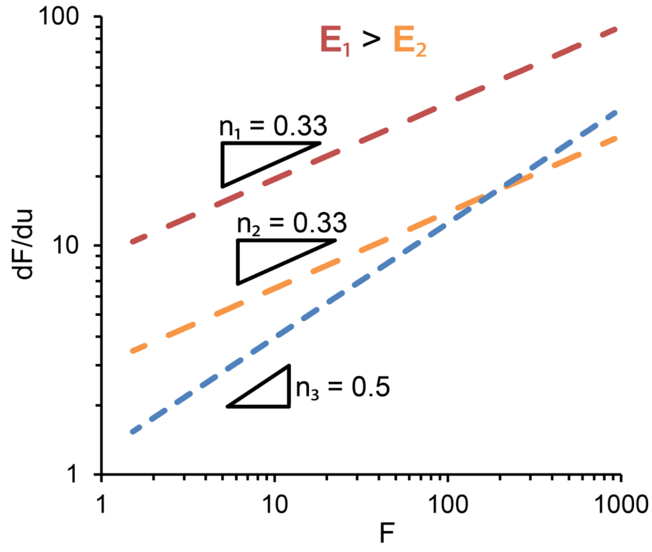

FIG. 4. Example log-log plot using the Garcia method. In this plot, a power-law relation is represented as a straight line, where the slope represents *n*, which is directly related to the power relationship between force and displacement. The vertical position of the data is determined by the magnitude of the reduced modulus—higher moduli model lines are translated higher along the *y* axis. In this example, the red and orange dashed lines represent the ideal Hertzian contact solution, where the modulus of the red contact response is larger than that of the orange. The blue line represents the Winkler contact model. However, moduli from lines of different *n* must be compared against the form of the analytic model in order to conclusively determine which has a stiffer response.

$$F = \frac{4}{3}E^{*}R^{\frac{1}{2}}(d - d_o)^{\frac{3}{2}}, \tag{1}$$

$$\frac{1}{E^{*}} = \frac{1 - \nu_1^2}{E_1} + \frac{1 - \nu_2^2}{E_2}. \tag{2}$$

The error for the Garcia dF/du versus force plots was determined for each metric. The magnitude of the force error is the average standard deviation of the variance of the ten averaged force measurements used for each plotted force point. The magnitude of the error in dF/du is calculated using error propagation on the forward difference of force divided by displacement. We assume no correlation in the measurements and use the simplified form of Eq. (3). For the quantity dF/du, this is calculated using Eq. (4),

$$U(f(x_1, x_2, \ldots, x_n))^2 = U(A)^2 = \sum_{i=1}^{n}\left(\frac{d}{dx_i}A\right)^2 U(x_i)^2, \tag{3}$$

$$\begin{aligned} U\left(\frac{dF}{du}\right)^2 &= U\left(\frac{F_2 - F_1}{u_2 - u_1}\right)^2 \\ &= \left(\frac{d}{dF_2}\frac{F_2 - F_1}{u_2 - u_1}\right)^2 U(F_2)^2 + \left(\frac{d}{dF_1}\frac{F_2 - F_1}{u_2 - u_1}\right)^2 U(F_1)^2 \\ &\quad + \cdots. \end{aligned} \tag{4}$$

2. Creep

Long-duration force-controlled experiments were conducted to view contact area expansion over time. A fixed normal load of 500, 750, or 1000 μN was applied by the probe onto the gel substrate for at least 600 s. This load was servo-ed in real time, allowing the tribometer vertical stage to adjust to maintain the prescribed load.

Image frames from the microscope video output were taken at 30 s intervals up to 180 and 60 s intervals thereafter for a total of 14 area measurements. Based on the observed speed of contact expansion, this variable interval was deemed sufficient to capture the area change over time. Creep experiment contact areas were measured using the methods outlined previously. These data points were then fit to an exponential model [Eq. (5)] to determine the time constant τ associated with the contact area expansion,

$$A = A_f + (A_o - A_f)\, e^{-t/\tau}, \tag{5}$$

$$\tau_P \approx \frac{a^2}{D_{SS}}. \tag{6}$$

There are two relaxation mechanisms of interest for soft polymer hydrogels: viscoelasticity and poroelasticity. Both mechanisms affect the contact response of the hydrogel, and determining the relative degree of one of them that occurs within the gradient layer will inform us of the probable structure of the layer. To understand which of these mechanisms were occurring within the hydrogel contact, we utilized theory developed by Hu and co-workers,[52,53] which can identify the primary relaxation mechanism based on the relationship of the obtained time constants with the applied load. In poroelastic theory, the time constants associated with the squeeze-out of water from the pores are dependent on the pore size and, therefore, a length scale of the contact. In particular, Hu obtained that the poroelastic relaxation time τ_P is related to the contact radius a of an indenter pushed into a porous substrate [Eq. (6)]. This is in contrast to viscoelasticity, where the relaxation time is only related to the shear modulus of the material and is wholly independent of any experiment length scale.[54] Therefore, a plot of the obtained time constants versus the contact length scale reveals the dominant mechanism and allows calculation of the diffusion coefficient based on the slope of a linear fit (Fig. 5). If the slope is close to zero, then the relaxation is primarily viscoelastic; if there is a significant slope, then the relaxation is primarily poroelastic. A steady-state diffusion coefficient can be calculated from the inverse of the slope produced by the time constants plotted versus the initial contact radius.[55] We fit time constants to each experiment's data of contact area versus time using least-squares regression (Excel Solver).

III. RESULTS

A. Indentation results

Indentations of all five compositions were analyzed by first applying the Garcia method for composition 3 (M7.5, R25), as it can be considered the most "standard" composition of the five based on the number of previous literatures surrounding it.[38,48,52,56,57] Using the Garcia method, we found that the contact behavior for this composition does not exhibit behavior indicative of a single suitable contact model or a single power-law fit. Immediately after the point of first contact, we observed the greatest variability in the data and any potential exponential fit, with values ranging from 0.3 to 0.8. We predict that this region of variability is due to squeeze-out of the water held by the loose polymer segments, which causes a ramping-up force response due to pressurization of the released water while it escapes the contact. After this initial variability, we could fit a portion of the contact to the Fredrickson high-penetration brush model,[58,59] which had $n = 0.67$ (Fig. 6). In this model, the force response is related to the shear modulus of the polymer chains G and their grafting density H [Eq. (7)]. After this interval, the next portion of each indentation curve fits well to a Winkler "bed-of-springs" contact model [see supplementary material, Eq. (2)], suggesting that the compression of the outermost brush segments did not induce significant strain in the material adjacent to it.[60] Beyond the Winkler-fitting region, we were able to fit a Hertz contact model to the rest of the points, which implies that the compressed gradient-density surface layer had begun to emulate the response of the well-cross-linked bulk. Previous indentations on pAam hydrogels showed that hydrogels molded against glass surfaces exhibited Hertzian contact mechanics,[39,52,56,61] supporting our assumption that the latter portions of each indentation would fit well to a Hertzian contact model,

$$F = \frac{192}{\pi^2} G \frac{R^2}{H^3} (d - d_o)^3. \tag{7}$$

The intersection between the Winkler-fitting region and the Hertz-fitting region occurs at a point we define as d_{match}. We can

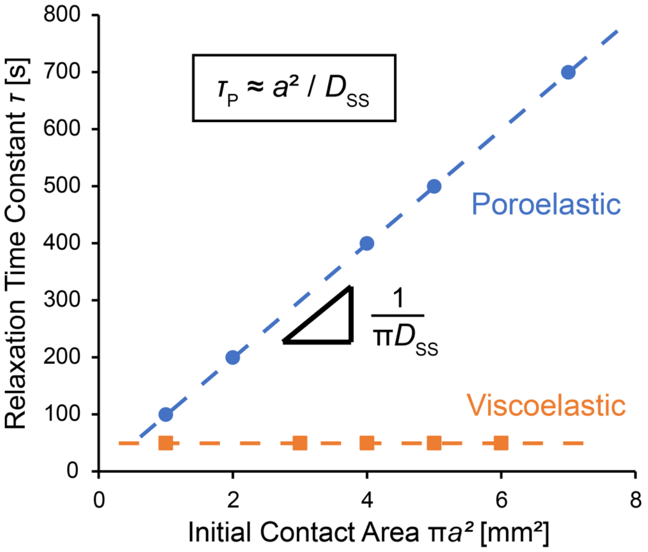

FIG. 5. Example plot of exponential time constants vs the contact area. When the time constant of relaxation correlates with the contact pressure and, therefore, the contact area, this indicates poroelastic relaxation. Alternatively, if the time constant is unchanged by varying the pressure/area, the relaxation is viscoelastic.

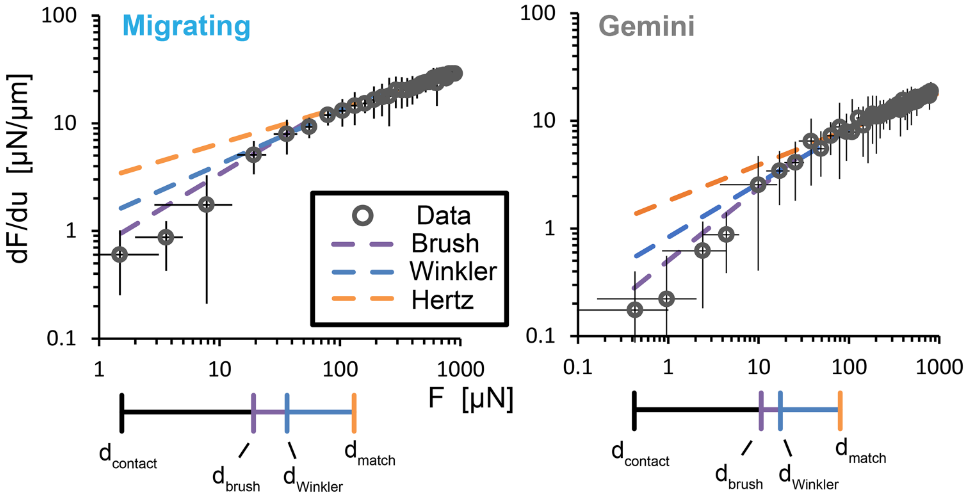

FIG. 6. Indentations at peak loads of 1000 μN for soft-substrate contact (left) and Gemini contact (right) setups. The dashed purple line corresponds to a brush contact model. In dashed blue is the Winkler contact model and in dashed orange is the Hertzian contact model. The data corresponding to each model are marked on the bottom line, with demarcations for transitions between models. The distance spanned by the entire line, from $d_{contact}$ to d_{match}, is equal to the gradient-layer thickness Δd. Error bars are shown for the force (horizontal, 5–14 μN) and dF/du (vertical, 1.6–8.2 μN/μm).

establish the contact-perceived thickness of the gradient layer as the probe indentation depth from the video-derived point of first contact $d_{contact}$ until the first point of the Hertzian-fitting region d_{match}—we term this distance as Δd. The magnitude of Δd can be considered the penetration depth after first contact before the Hertz contact model applies. Because it spans the substrate thickness before Hertz contact fits, it provides a rough estimate of the thickness of the gradient layer, which is how we will refer to this measure hereafter. This shows that the thickness of the gradient layer for our standard composition hydrogel is roughly 17.1 μm thick (see Table II), which is within the proposed 10–20 μm range estimated via neutron reflectometry.[34,35] Of this thickness, approximately 80% of this distance comprises the brush-fitting and Winkler-fitting region, which indicates the degree of "brushiness" as a function of the penetration depth: a higher percentage corresponds to the presence of loosely cross-linked chains further into the depth. The Gemini contact had a gradient-layer thickness of 25.3 μm—47% larger than the soft-substrate case, and the portion of each indentation corresponding to a brush-fitting or Winkler-fitting region dropped to 67% for a Gemini contact configuration.

When the indentations are plotted in a log-log format, it becomes apparent that measurement error alone cannot account for the non-Hertzian region. In Fig. 6, error bars appear nonsymmetric due to the log-log scaling, which means that it is more difficult for a low dF/du response, such as what is demonstrated in the figure, to be an erroneous measurement of a dF/du response roughly half a magnitude higher. Thus, usage of the Garcia method strongly reinforces the non-Hertzian determination of the initial response from the gradient-surface layer.

TABLE II. Elastic moduli, gradient-layer thickness Δd, and portion of the gradient-layer thickness interval corresponding to a Winkler model for each contact setup.

Contact setup	Elastic modulus E (kPa)	Gradient-layer thickness Δd (μm)	Winkler % of Δd
Soft-substrate	33.8	17.1	79.5
Gemini	33.1	25.3	66.9

It is important to note that the contact area observed throughout each indentation also deviated from a single contact model estimation. For example, using the probe displacement to predict a contact area using Hertzian contact mechanics would underpredict the actual contact area of these gradient-layered hydrogels by as much as 44% (see Fig. 7). If we instead use a piece-wise analytic

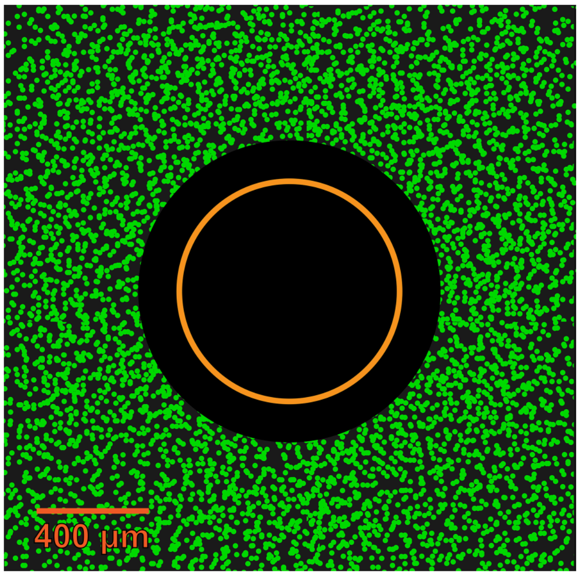

FIG. 7. Illustration of a representative contact area projection observed using particle exclusion microscopy. The orange circle represents the expected contact area from a Hertzian contact model prediction, which underpredicts the actual contact area by as much as 44%.

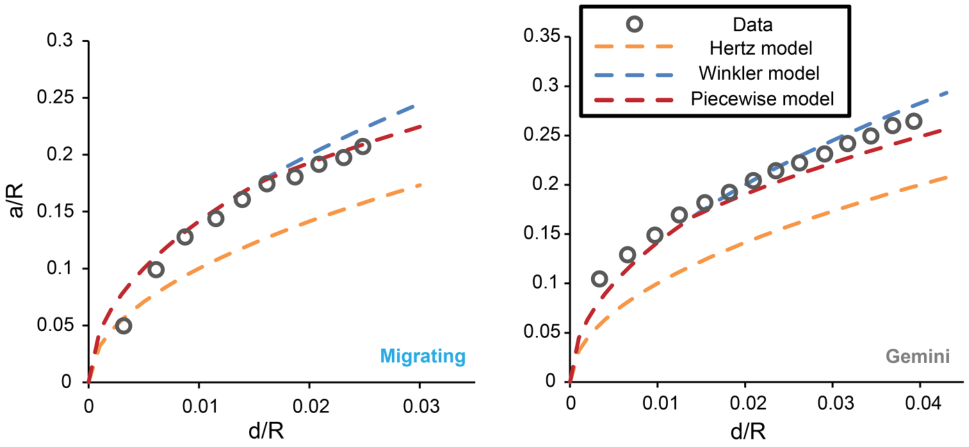

FIG. 8. Compatibility plot of a/R vs d/R for both indentations of Fig. 6. In dashed blue is the predicted compatibility relationship solely using a Winkler model. In dashed orange is the predicted compatibility solely using a Hertzian contact model. The red dashed line is an analytic prediction using a Winkler model for the probe displacement spanning Δd and a Hertzian model afterward. This validates the need for multiple contact models to fully describe the contact.

model, where we use a Winkler model for the probe displacement d spanning the gradient-layer thickness Δd and a Hertzian contact model for values after that, we obtain a prediction of the contact radius that is much closer to that observed experimentally (Fig. 8). We note that this fit is not perfect since we have assumed a Winkler contact model through the initial indentation regime where brush contact and fluid squeeze-out, not Winkler contact, are the prevalent behavior; deriving contact areas for these phenomena would improve the predicted contact area fit.

Next, the indentations of the other four compositions with variations in monomer and cross-linker were analyzed using the Garcia method to infer the influence of hydrogel composition. Elastic moduli for each composition were calculated using the Garcia analysis method's K coefficient, which was found using a single-parameter least-squares fitting of a Hertzian contact model to the high-displacement data. The resulting elastic moduli are listed in Table III. The total polymer concentration M had a larger effect on the elastic modulus compared to the cross-linker ratio R. In fact, the effect of increasing cross-linker concentration (decreasing R) appears to have diminishing returns: a 67% increase in the available cross-linker increased the modulus by only 19%, while a 90% reduction in the cross-linker reduced the modulus by 92%. This suggests that cross-linking is potentially inhibited by self-linking of the bisacrylamide, which has been predicted to be the predominant polymer structure for hydrogels with high concentrations of the cross-linker.[62]

After fitting the Hertzian regime of each indentation, we then determined regions of each indentation that corresponded to Winkler contact [see supplementary material, Eq. (2)] or Frederickson's high-penetration brush model [Eq. (7)].[58] In every experiment, we found portions of the indentation data that fit these models (see the supplementary material[68]), which means that changes to the composition cannot eliminate the "brushy" layer of pAam hydrogels molded against polystyrene. This additionally shows that the progressive contact modeling of the gradient layer for composition 3 holds true for all compositions. Early portions of the indentation data of the stiffer compositions 3–5 (R25, M15, R15) had a higher slope as large as $n = 0.9$, which may be attributed to pressurization of water within the gradient layer that is unable to vacate the contact in time due to poroelastic pressure. The thickness of the gradient layer for each composition, Δd, was different for each composition (Table III). For all compositions and setups, the thickness was between 10 and 40 μm, which is similar to the order of magnitude predicted by Simič *et al.*[63] For changing monomer percent M and constant ratio R (compositions 2–4), the gradient-layer thickness was correlated with monomer percent M, with composition 2 having the largest gradient layer and composition 4 having the smallest one. The portion of the gradient layer corresponding to a brush or Winkler contact model was the largest for composition 2 at 89% and decreased to 67% for composition 4. Similar trends were obtained for a reduction in the monomer-to-cross-linker ratio R, where a gradient-layer

TABLE III. Composition number and their corresponding elastic moduli determined from indentation experiments. The indentation-derived gradient-layer thickness, Δd, is also listed for each contact setup.

Comp no.	Elastic modulus E (soft-substrate) (kPa)	Elastic modulus E (Gemini) (kPa)	Gradient-layer thickness Δd (soft-substrate) (μm)	Gradient-layer thickness Δd (Gemini) (μm)
1 (R250)	2.42	2.84	43.7	9.6
2 (M5)	7.26	6.36	21.4	4.9
3 (M7.5,R25)	33.8	33.1	17.1	25.3
4 (M15)	169.7	153.1	13.4	17.1
5 (R15)	40.1	38.7	12.7	18.8

thickness of 43.7 μm was found for composition 1 (R250), while composition 5 (R15) only had a layer thickness of 12.7 μm. The portion of the gradient layer that followed brush or Winkler contact modeling was 89% for composition 1 and 63% for composition 5. Thus, for all soft-substrate contact experiments, the proportion of the Δd interval corresponding to a brush-fitting or Winkler-fitting region increased for larger gradient-layer thicknesses. This also hints that both composition metrics M and R are influential on the resulting gradient-layer structure.

However, the results from the Gemini contact were not as predictable. While we saw larger gradient-layer thicknesses perceived for compositions 3–5 compared to their soft-substrate contact values, compositions 1 and 2 showed smaller gradient-layer thicknesses. The Gemini contact perceived gradient layers of 9.6 and 4.9 μm for compositions 1 and 2, respectively. The portion of each Δd thickness interval corresponding to a brush or Winkler model was 100% for both compositions; the initial brush response in composition 1 (R250) is stiffer than the bulk response. In soft-substrate contact, these two compositions showed thick gradient layers with a high percentage consisting of brushy behavior.

B. Creep results

Creep experiments confirmed an increase in the contact area with time, which corresponded to a pressure decrease with time (Fig. 9). The majority of contact area gain occurred within the first 200 s regardless of the contact setup. In general, smaller loads experienced greater area growth by percentage compared to larger loads. Area expansion was larger in the Gemini contact compared to the hard-probe setup. The softer two compositions (1,2) relaxed to a greater degree than the other compositions when under low loads but saw the greatest discrepancy between low-load and high-load relaxation (Table IV). Particularly in self-mated contact, we postulate that the initial probe deformation reduced the capacity for the contact to relax over time.

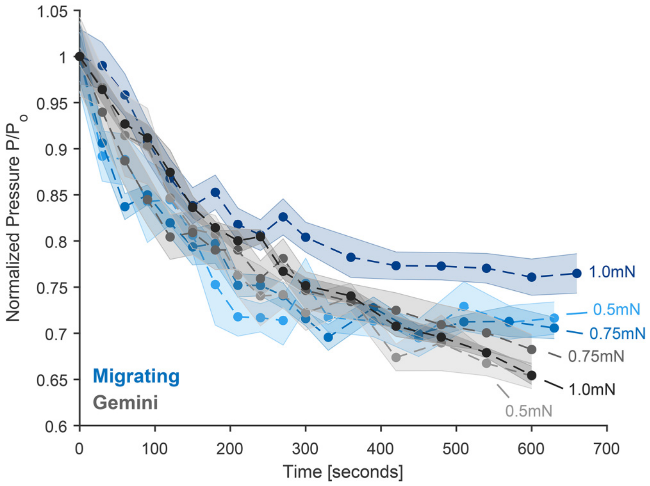

FIG. 9. Pressure vs time for both soft-substrate contact (blue) and Gemini contact (gray) setups on composition 3 at three different normal loads. Pressure drops more substantially in lightly loaded contacts.

When fitting the area growth curves to exponential functions and extracting time constants, we were able to show that the time constants varied significantly with the initial contact radius, which is a function of the applied load/initial pressure (see Fig. 10). The inverse of the slope created by the time constant trend with the contact radius produced a steady-state diffusion coefficient for each contact setup.[55] For composition 3 in a soft-substrate contact setup, this was $12.4 \times 10^{-10}\ \mathrm{m}^2/\mathrm{s}$, while the Gemini contact had a coefficient value of $7.51 \times 10^{-10}\ \mathrm{m}^2/\mathrm{s}$. Both of these values are close to reported coefficients in previous studies of pAam hydrogel poroelasticity, which had a diffusion constant of $5 \times 10^{-10}\ \mathrm{m}^2/\mathrm{s}$.[52] This, as well as the variation in the time constant magnitude with the initial contact radius, proves that poroelastic squeeze-out was the primary driver of the contact area expansion. This aligns with previous studies that have shown a low degree of viscoelastic relaxation versus poroelastic relaxation.[45]

Creep experiments on the other four compositions showed a time constant variation with the initial applied pressure, also suggesting poroelastic-dominated relaxation made possible by a less-dense, less-cross-linked surface layer. The only exception to this behavior was composition 1, which we had initially predicted to show viscoelastic-dominant behavior.[46] Composition 1, with a cross-linker ratio of $R = 250$, showed consistent time constants with varying normal load/contact radii, indicative of viscoelastic-dominant relaxation behavior. This means that, while poroelastic squeeze-out was likely to also be occurring, it was not as significant of a contributor to the area expansion as the viscoelastic stress relaxation throughout the gel. Diffusion coefficients were calculated using the slope produced by the time constants (Table V). These coefficients give a measure of the relative mobility of the water within the gel and particularly within the gradient layer. In general, the steady-state diffusion coefficient decreased for stiffer compositions, i.e., for larger M and smaller R. This aligns with the results from indentation, which showed thinner gradient layers for stiffer compositions, which reduces the amount of water that can be exuded under pressures below the osmotic pressure of the bulk cross-linked structure. In composition 3, we see values 50%–100% larger than those found in the previous work on glass-molded

TABLE IV. Contact area expansion compared to the initial contact for both contact configurations and for the minimum and maximum loads. Minimum loads experienced larger contact growth % compared to maximum loads.

Comp no.	Area expansion (min load) (soft-substrate) (%)	Area expansion (max load) (soft-substrate) (%)	Area expansion (min load) (Gemini) (%)	Area expansion (max load) (Gemini) (%)
1	69.2	44.3	68.3	17.6
2	80.2	22.2	103.1	51.1
3	45.3	38.3	71.0	51.3
4	54.5	68.1	39.6	47.4
5	51.8	44.3	68.2	50.9

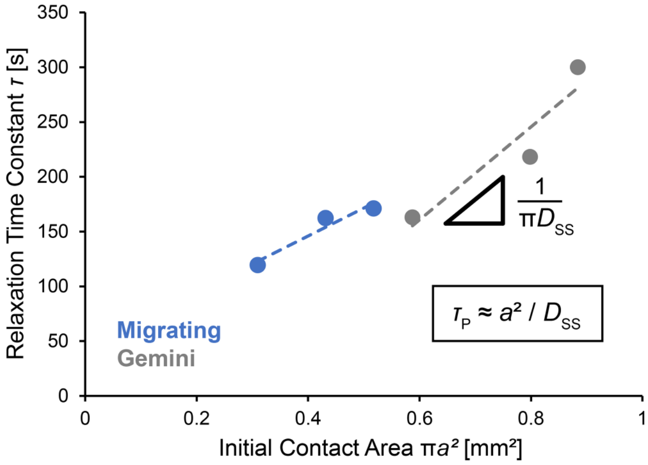

FIG. 10. Time constants obtained from fitting exponential models for both soft-substrate (blue) and Gemini contact (gray). In both contact setups, the associated time constant of relaxation differed based on the applied load. Steady-state diffusion coefficients were calculated from the inverse of the slope created by the varying time constants.

pAam gels of identical chemical composition ($5*10^{-10}$ m^2/s);[52] this further supports the theory of increased water mobility within the gradient layer.

IV. DISCUSSION

A. Gradient-layer contact mechanics

Through indentation experiments, we have demonstrated that Gombert and Meier's prediction of a gradient-surface layer for these hydrogels molded against polystyrene is true.[34,35] More than that, we show that this gradient layer alters the contact response such that it can only be described using different contact models with increasing depth: initial contact is controlled by fluid pressurization and squeeze-out, followed by brushlike contact, then the Winkler contact, and finally the Hertzian contact at sufficient indentation depths (Fig. 11). The accuracy of these contact model fits reinforces the notion of an evolving polymer structure at the interface as the probe pushes into the substrate. The contact is first controlled by water squeeze-out from the sparse chains at the surface, which would be composed of loosely cross-linked acrylamide backbone chains extended outward toward the good solvent bath. The resulting structure would resemble a polymer brush of increasing density as the probe traveled further into the substrate. Further indentation and interaction with those chains would then produce a response similar to deep polymer brush contact. Eventually, compression of these polymer segments induces a "bed-of-springs" response, where the polymer chain contact with the probe is more uniformly distributed, but compressed chains do not yet interact with neighboring chains. Eventually, the chains are compressed to the point that their response emulates that of the well-cross-linked bulk. While Hertzian contact mechanics has an upper limit on viability based on substrate thickness and probe size, these findings establish a lower limit on the applicability of Hertzian contact for hydrogels possessing a significant graded surface layer. Consideration of brush-type and Winkler-type contact must additionally be accounted for in order to accurately predict the contact behavior of the interface. However, it should be noted that we were unable to decisively determine appropriate contact models for all portions of the gradient-layer thickness Δd. In the work by Williams, it is expected that the low-penetration and high-penetration brush models should intersect at a transition point.[59] Our data show no obvious transition, with power-law fits in the region between $d_{contact}$ and d_{brush} that exceed Fd^3. While we propose the reason behind this large force-depth relationship to be caused by fluid pressurization, we lack the data to conclude this. Future work could potentially solve this question using faster acquisition or quicker imaging techniques.

TABLE V. Diffusion coefficients obtained from exponential fitting of the area relaxation of each experiment for both contact setups. Composition 1 experienced a far greater degree of viscoelasticity compared to the other four compositions.

Comp no.	D_{SS} (soft-substrate) (10^{-10} m^2/s)	D_{SS} (Gemini) (10^{-10} m^2/s)
1	N/A	82.3
2	10.4	20.0
3	12.4	7.51
4	3.16	10.1
5	6.70	6.62

For a Gemini contact setup, we showed anomalous behavior occurring for the most compliant compositions 1 and 2, where the gradient-layer thickness was supposedly less than the stiffer compositions. The reason for this can be attributed to the interaction method between the two gradient layers. In a good solvent, it has been shown that acrylamide and bisacrylamide segments are unlikely to become entangled in a self-mated contact configuration, as they prefer instead to extend into the surrounding water.[38,57,64,65] Williams, following up on Fredrickson's brush contact model, proposed that at low probe penetration depths, a rigid probe indenting into a polymer brush would experience a Hertzian force-depth relationship of $Fd^{\frac{3}{2}}$ based on the stiffness of the brush.[59] In the Gemini contact, these two combined findings would result in a larger portion of the indentation curve, including immediately after the initial contact, to experience Hertz-like contact. For the Gemini contact, we see a major constriction and near-elimination of this non-Hertzian region for these two softer compositions, implying that the physical interaction between the identical low-density gradient layers is not dissimilar to a response from the bulk. This makes the low-penetration brush contact model by Williams, which is essentially the Hertzian contact, a more accurate descriptor at the onset of contact. Second, if the stiffness of the brush is close to the stiffness of the bulk polymer, then the Hertzian response at the onset of contact will blend with the Hertzian response of the bulk and constrict the apparent gradient-layer thickness. Additionally, the high-penetration brush model and the Winkler model will have larger relative stiffnesses compared to the bulk stiffness since their stiffness is related to the

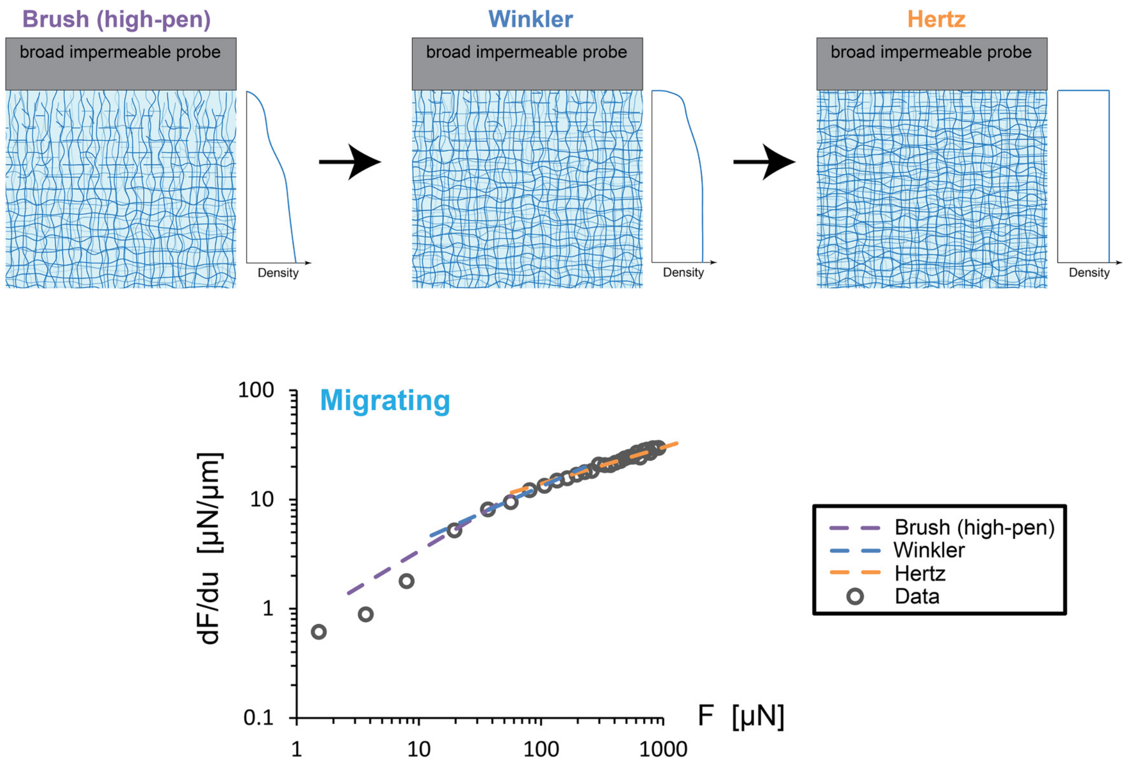

FIG. 11. Polymer structure contacting the indenter evolves with penetration depth, which can be adequately described by a piecewise contact model. As the gradient layer of the hydrogel is compressed, the dominant contact model progresses from brushlike to Winkler bed-of-springs-like to Hertzian. Shown here is a soft-substrate contact setup.

stiffness of the polymer chains making up the polymer "brush" at the surface. In fact, we find that the brush stiffness in composition 1 is larger than the response generated by the bulk. This means that the captured water is primarily responsible for the rigidity of the hydrogel, which is lost when the water is exuded under pressure. Fitting low-penetration brush models to the stiffer three compositions gives a brush stiffness of 2.4 kPa for composition 3, 3.6 kPa for composition 4, and 3.8 kPa for composition 5. Despite the vast differences in bulk stiffness, the magnitude of the brush layer stiffness is similar across compositional changes. This would suggest that, while the gradient-layer thicknesses of compositions 1 and 2 may be larger, the stiffness of the brush and the bulk are close enough that distinguishing them from each other is difficult.

These experiments have demonstrated how the thickness of the gradient-surface layer is highly dependent on both composition parameters of the polyacrylamide hydrogel system. Looking at the gradient-layer thickness as measured by the soft-substrate contact, doubling the total polymer percent M results in only a 22% decrease in the gradient-layer thickness (Fig. 12). In comparison, a 40% decrease in the monomer-to-cross-linker ratio R results in a 26% decrease in the gradient-layer thickness. This can be attributed to the dependence of bisacrylamide for cross-linking, causing a greater degree of bisacrylamide to decrease the average length and density of uncross-linked chains comprising the less-dense surface. Gombert suggests that the dominant network structure of polyacrylamide consists of large bisacrylamide clusters,[62] which would be particularly sensitive to alterations to the cross-linker content. As oxygen permeation from the substrate is responsible for hindrance of the bisacrylamide bonding,[36] a relative abundance of bisacrylamide within the polymerizing solution will counter the effect of the oxygen. As such, the thickness of the gradient layer is more sensitive to changes in the monomer-to-cross-linker ratio R than the total polymer percent M, but both affect the resulting gradient layer.

B. Gradient-layer relaxation

Creep experiments showed that the dilute nature of the gradient layer allows it to poroelastically exude water under unexpectedly low pressures. A key demonstration of this are the creep experiments on composition 3, where the maximum pressure of any single creep experiment was only 1.8 kPa, while the osmotic pressure of a well-cross-linked hydrogel of the same composition has been reported to be 11 kPa.[66,67] Despite applying a max pressure of only 7% of the osmotic pressure of the bulk, we showed that the dominant method of relaxation was poroelastic squeeze-out. This discrepancy is explained by the dilute nature of the gradient layer, which, at its periphery, is composed of dangling chains holding water that is easily displaced. The graded nature of the surface is

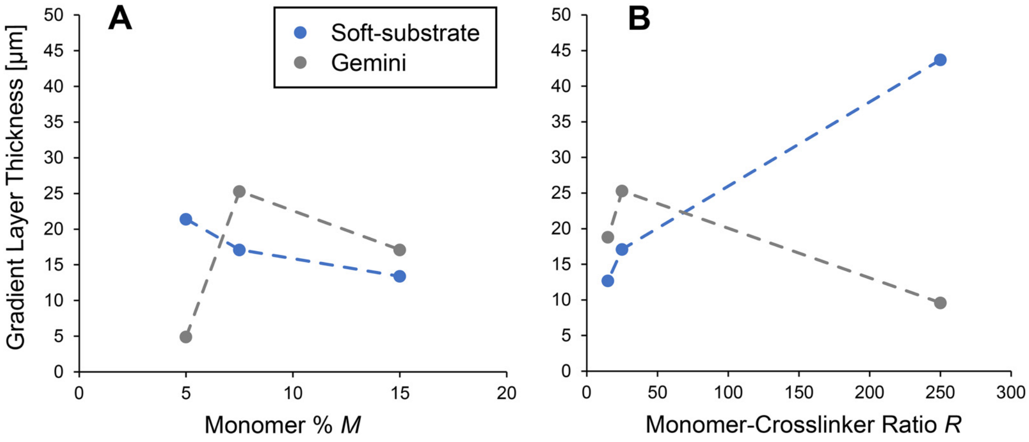

FIG. 12. (a) Gradient-layer thickness measured either through soft-substrate or Gemini contact configurations for compositions with varying total polymer percent *M* and fixed monomer-to-cross-linker ratio ($R = 25$). (b) Gradient-layer thickness for compositions with different monomer-to-cross-linker ratio *R* but identical monomer percent ($M = 7.5\%$).

expected to have varying osmotic pressures through its thickness, as the pore size is inversely related to the degree of cross-linking,[39] and the pore size is directly linked to the osmotic pressure magnitude. As a result, the lower degree of cross-linking within the gradient layer causes far lower osmotic pressures within it that allow local poroelastic squeeze-out to occur under vanishingly small pressures. The advent of poroelastic-dominated relaxation within the gradient layer may be surprising considering the higher degree of viscoelasticity observed in comparatively dilute hydrogels.[49] However, compared to their uniform hydrogels, the strain applied to our graded hydrogels is not well-distributed, as the more compliant surface layer will preferentially stretch to accommodate the pressure within itself compared to the bulk structure. When this compression is combined with the time-dependent relaxation of the applied pressure through the network, the locally increased pressure can lead to water exudation from the gradient layer. The use of embedded particles in a hydrogel to monitor the strain within the gradient layer under load could be used to prove this conclusively. However, one would require a very efficient equipment setup to scan confocal volumes at a rate faster than the rate of relaxation.

V. CONCLUSIONS

Indentation experiments confirmed the presence of a “brushy” gradient layer for all compositions, with the more compliant compositions (1, 2) exhibiting the largest gradient-layer thicknesses as measured using a soft-substrate contact setup. Non-Hertzian regimes were observed at the earliest stages of each indentation. The full contact response could be adequately predicted using piecewise contact modeling using three models: the high-penetration brush contact, the Winkler contact, and the Hertzian contact. This modeling supports findings by Meier *et al.*, who found that the “brushy” gradient-surface layer has a lower density of polymer and cross-links (and, therefore, a higher proportion of water) compared to the bulk network.

Creep experiments showed that compositions 2–5 were able to experience localized poroelastic relaxation within the gradient layer thanks to its relative polymer sparsity. Composition 1 showed viscoelastic-dominant relaxation, showing how a severe lack of cross-linking creates a gradient layer that responds more like the bulk than other compositions.

These findings provide useful information about the contact response of hydrogels with gradient-density surface layers and how to alter it via composition changes. This link will allow hydrogel designs intentionally incorporating a gradient-surface layer to achieve a desired contact and relaxation response in tribological applications.

ACKNOWLEDGMENTS

The authors are grateful for the inspirational work of Nicholas Spencer as well as excellent stories and encouragement to follow curiosity to discover something new. Thanks very much to the Materials Tribology Laboratory members for discussions and early reviews. This work was funded by the National Science Foundation (Award No. 1751945).

AUTHOR DECLARATIONS

Conflict of Interest

The authors have no conflicts to disclose.

Ethics Approval

Ethics approval is not required.

Author Contributions

Christopher L. Johnson: Conceptualization (equal); Data curation (lead); Funding acquisition (lead); Methodology (equal); Project administration (equal); Resources (lead); Software (lead);

Supervision (lead); Writing – original draft (lead); Writing – review & editing (supporting). **Alison C. Dunn:** Conceptualization (equal); Data curation (lead); Funding acquisition (lead); Methodology (equal); Project administration (equal); Resources (lead); Software (lead); Supervision (lead); Writing – original draft (lead); Writing – review & editing (lead).

DATA AVAILABILITY

The data that support the findings of this study are available from the corresponding author upon reasonable request.

REFERENCES

[1] N. A. Peppas and C. T. Reinhart, J. Membr. Sci. **15**, 275 (1983).

[2] A. A. Pitenis, J. M. Urueña, A. C. Cooper, T. E. Angelini, and W. G. Sawyer, J. Tribol. **138**(4), 042103 (2016).

[3] A. S. Hoffman, Adv. Drug Deliv. Rev. **54**, 3 (2002).

[4] B. D. Ratner and A. S. Hoffman, "Synthetic hydrogels for biomedical applications," Hydrogels for Medical and Related Applications, ACS Symposium Series Vol. 31 (American Chemical Society, Washington, DC, 1976), pp. 1–36.

[5] O. Wichterle and D. Lím, Nature **185**, 117 (1960).

[6] P. Calvert, Adv. Mater. **21**, 743 (2009).

[7] J. L. Drury and D. J. Mooney, Biomaterials **24**, 4337 (2003).

[8] D. DeRossi, K. Kajiwara, Y. Osada, and A. Yamauchi, J. Chem. Inf. Model. **53**, 289 (1991).

[9] S. H. Kim, C. Marmo, and G. A. Somorjai, Biomaterials **22**, 3285 (2001).

[10] A. C. Dunn, J. A. Cobb, A. N. Kantzios, S. J. Lee, M. Sarntinoranont, R. Tran-Son-Tay, and W. G. Sawyer, Tribol. Lett. **30**, 13 (2008).

[11] A. C. Dunn, J. M. Urueña, E. Puig, V. L. Perez, and W. G. Sawyer, Tribol. Lett. **49**, 145 (2013).

[12] H. Pult, S. G. Tosatti, N. D. Spencer, J. M. Asfour, M. Ebenhoch, and P. J. Murphy, Ocul. Surf. **13**, 236 (2015).

[13] M. Samsom, A. Chan, Y. Iwabuchi, L. Subbaraman, L. Jones, and T. A. Schmidt, Tribol. Int. **89**, 27 (2015).

[14] S. M. Hart, E. O. Mcghee, J. Manuel, U. Padraic, P. L. Stephen, M. A. Schaller, A. A. Pitenis, and W. G. Sawyer, Tribol. Lett. **68**, 106 (2020).

[15] O. Sterner, C. Karageorgaki, M. Zürcher, S. Zürcher, C. W. Scales, Z. Fadli, N. D. Spencer, and S. G. Tosatti, ACS Appl. Mater. Interfaces **9**, 20150 (2017).

[16] I. L. Kim, R. L. Mauck, and J. A. Burdick, Biomaterials **32**, 8771 (2011).

[17] M. Freeman, M. Furey, B. Love, and J. Hampton, Wear **241**, 129 (2000).

[18] K. L. Spiller, S. A. Maher, and A. M. Lowman, Tissue Eng. Part B **17**, 281 (2011).

[19] C. M. Beddoes, M. R. Whitehouse, W. H. Briscoe, and B. Su, Materials **9**, 443 (2016).

[20] F. Li, A. Wang, and C. Wang, J. Mater. Sci.: Mater. Med. **27**, 87 (2016).

[21] Y. Shi and D. Xiong, Wear **305**, 280 (2013).

[22] M. M. Blum and T. C. Ovaert, Mater. Sci. Eng., C **33**, 4377 (2013).

[23] M. A. Haque, T. Kurokawa, and J. P. Gong, Polymer **53**, 1805 (2012).

[24] R. Crockett, A. Grubelnik, S. Roos, C. Dora, W. Born, and H. Troxler, J. Biomed. Mater. Res. Part A **82**, 958 (2007).

[25] E. D. Bonnevie, V. J. Baro, L. Wang, and D. L. Burris, J. Biomech. **45**, 1036 (2012).

[26] J. P. Gong, Y. Katsuyama, T. Kurokawa, and Y. Osada, Adv. Mater. **15**, 1155 (2003).

[27] J. Y. Sun, X. Zhao, W. R. Illeperuma, O. Chaudhuri, K. H. Oh, D. J. Mooney, J. J. Vlassak, and Z. Suo, Nature **489**, 133 (2012).

[28] P. Lin, S. Ma, X. Wang, and F. Zhou, Adv. Mater. **27**, 2054 (2015).

[29] Y.-S. Pan, D.-S. Xiong, and R.-Y. Ma, Wear **262**, 1021 (2007).

[30] Y. Pan and D. Xiong, Wear **266**, 699 (2009).

[31] A. A. Pitenis, J. M. Urueña, R. M. Nixon, T. Bhattacharjee, B. A. Krick, A. C. Dunn, T. E. Angelini, and W. G. Sawyer, J. Tribol. **138**, 042102 (2016).

[32] A. Kii, J. Xu, J. P. Gong, Y. Osada, and X. Zhang, J. Phys. Chem. B **105**, 4565 (2001).

[33] J. P. Gong, Soft Matter **2**, 544 (2006).

[34] Y. A. Meier, K. Zhang, N. D. Spencer, and R. Simic, Langmuir **35**, 15805 (2019).

[35] Y. Gombert, R. Simič, F. Roncoroni, M. Dübner, T. Geue, and N. D. Spencer, Adv. Mater. Interfaces **6**, 1901320 (2019).

[36] R. Simič, J. Mandal, K. Zhang, and N. D. Spencer, Soft Matter **17**, 6394 (2021).

[37] Y. Lai, D. He, and Y. Hu, Extreme Mech. Lett. **31**, 100540 (2019).

[38] J. M. Urueña, A. A. Pitenis, R. M. Nixon, K. D. Schulze, T. E. Angelini, and W. Gregory Sawyer, Biotribology **1–2**, 24 (2015).

[39] J. M. Urueña, E. O. McGhee, T. E. Angelini, D. Dowson, W. G. Sawyer, and A. A. Pitenis, Biotribology **13**, 30 (2018).

[40] T. Shoaib and R. M. Espinosa-Marzal, Tribol. Lett. **66**, 1 (2018).

[41] T. Shoaib, J. Heintz, J. A. Lopez-Berganza, R. Muro-Barrios, S. A. Egner, and R. M. Espinosa-Marzal, Langmuir **34**, 756 (2018).

[42] T. Shoaib and R. M. Espinosa-Marzal, ACS Appl. Mater. Interfaces **11**, 42722 (2019).

[43] T. Shoaib and R. M. Espinosa-Marzal, Colloids Interfaces **4**, 54 (2020).

[44] S. Z. Bonyadi, M. M. Hasan, J. Kim, S. Mahmood, K. D. Schulze, and A. C. Dunn, Tribol. Lett. **68**, 119 (2020).

[45] M. Galli, K. S. Comley, T. A. Shean, and M. L. Oyen, J. Mater. Res. **24**, 973 (2009).

[46] J. Zhang, C. R. Daubert, and E. A. Foegeding, Rheol. Acta **44**, 622 (2005).

[47] C. L. Johnson and A. C. Dunn, Exp. Mech. **61**, 829 (2021).

[48] A. C. Dunn, J. M. Urueña, Y. Huo, S. S. Perry, T. E. Angelini, and W. G. Sawyer, Tribol. Lett. **49**, 371 (2013).

[49] E. O. McGhee, A. A. Pitenis, J. M. Urueña, K. D. Schulze, A. J. McGhee, C. S. O'Bryan, T. Bhattacharjee, T. E. Angelini, and W. G. Sawyer, Biotribology **13**, 23 (2018).

[50] K. D. Schulze, A. I. Bennett, S. Marshall, K. G. Rowe, and A. C. Dunn, J. Tribol. **138**, 041404 (2016).

[51] M. Garcia, K. D. Schulze, C. S. O'Bryan, T. Bhattacharjee, W. G. Sawyer, and T. E. Angelini, Tribol. Mater. Surf. Interfaces **11**, 187 (2017).

[52] E. P. Chan, Y. Hu, P. M. Johnson, Z. Suo, and C. M. Stafford, Soft Matter **8**, 1492 (2012).

[53] Z. I. Kalcioglu, R. Mahmoodian, Y. Hu, Z. Suo, and K. J. Van Vliet, Soft Matter **8**, 3393 (2012).

[54] M. Rubinstein and R. H. Colby, *Polymer Physics* (Oxford University Press, 2003), pp. 282–293.

[55] Y.-Y. Lin and B.-W. Hu, J. Non-Cryst. Solids **352**, 4034 (2006).

[56] Y. Hu, X. Zhao, J. J. Vlassak, and Z. Suo, Appl. Phys. Lett. **96**, 121904 (2010).

[57] A. A. Pitenis, J. M. Urueña, K. D. Schulze, R. M. Nixon, A. C. Dunn, B. A. Krick, W. G. Sawyer, and T. E. Angelini, Soft Matter **10**, 8955 (2014).

[58] G. H. Fredrickson, A. Ajdari, L. Leibler, and J. P. Carton, Macromolecules **25**, 2882 (1992).

[59] D. R. Williams, Macromolecules **26**, 5096 (1993).

[60] P. Põdra and S. Andersson, Wear **207**, 1–2 (1997).

[61] A. A. Pitenis and W. G. Sawyer, Tribol. Lett. **66**, 113 (2018).

[62] Y. Gombert, F. Roncoroni, A. Sánchez-Ferrer, and N. D. Spencer, Soft Matter **16**, 9789 (2020).

[63] R. Simič, M. Yetkin, K. Zhang, and N. D. Spencer, Tribol. Lett. **68**, 64 (2020).

[64] J. Klein, D. Perahia, and S. Warburg, Nature **352**, 143 (1991).

[65] M. K. Singh, P. Ilg, R. M. Espinosa-Marzal, M. Kröger, and N. D. Spencer, Tribol. Lett. **63**, 17 (2016).

[66] K. D. Schulze, S. M. Hart, S. L. Marshall, C. S. O. Bryan, J. M. Urueña, A. A. Pitenis, W. G. Sawyer, and T. E. Angelini, Biotribology **11**, 3 (2017).

[67] A. Bhattacharyya, C. O'Bryan, Y. Ni, C. D. Morley, C. R. Taylor, and T. E. Angelini, Biotribology **22**, 100125 (2020).

[68] See the supplementary material at https://www.scitation.org/doi/suppl/10.1116/6.0002047 for extended discussion of the tribometer setup, particle exclusion methodology, Garcia method application, and additional indentation results.